*Proceedings of the*
*Annual Stability Conference*
*Structural Stability Research Council*
*Louisville, Kentucky, April 1-4, 2025*

# Analytical investigation of plate buckling capacity under inelastic cyclic loading

Eman M.A. Abdullah[1], Andrew J. Ziccarelli[2]

**Abstract**
Due to steel's high strength-to-weight ratio, members are composed of slender elements, which can make them prone to local buckling—a failure mode that can lead to global instability or fracture due to high localized strains. There are concerns that the current AISC 341 slenderness limits do not lead to consistent seismic performance across members and systems. This research project aims to address this shortcoming by developing a mechanics-based predictive model for the buckling of steel plate members under seismic loading.

Using ABAQUS, we performed a comprehensive analytical study to investigate the strain capacity of plate elements subjected to inelastic cyclic loading. We compared the responses of plate elements under monotonic loading with those under various cyclic loading protocols to determine the onset of buckling. Our study examined the effects of plate slenderness ratio, applied loading protocol, and cyclic material model on the buckling behavior.

The findings reveal significant insights into the buckling behavior of steel elements under cyclic loading, highlighting the influence of boundary conditions, slenderness ratio and loading history. A simplified analytical model was developed to predict the occurrence of buckling. This fundamental knowledge is crucial for the AISC to develop and implement improved seismic compactness criteria, ensuring more consistent and predictable performance of steel structures in seismic conditions. This research contributes to the broader understanding of local buckling mechanisms, offering practical implications for the design and reliability of steel structures.

## 1. Introduction

Due to steel's high strength-to-weight ratio, the cross-sections of steel elements can be slender, making them susceptible to local buckling. This phenomenon becomes particularly critical in seismic conditions, where cyclic loading induces large localized strains and accelerates structural degradation. Local buckling not only compromises load-carrying capacity but can also lead to strain concentrations in the buckled areas, potentially causing fractures due to ultra-low cycle fatigue (Fell et al., 2009). The study by Torabian and Schafer (2014) demonstrated that slender plates exhibit significant out-of-plane deflections in the post-buckling regime. However, they can

[1] Graduate Research Assistant, NC State University, <eabdull@ncsu.edu>
[2] Assistant Professor, NC State University, <ajziccar@ncsu.edu>

still maintain some load-carrying capacity due to stress redistribution. Nonetheless, increased slenderness amplifies strain localization, which in turn accelerates progressive strength deterioration and can lead to fracture. Torabian and Schafer (2014) also emphasized the role of local slenderness in influencing the strain capacity and rotational behavior of steel members, highlighting that slenderness directly impacts not only the onset but also the progression of buckling and failure modes.

Slenderness may be defined as a dimensionless parameter, $\lambda$, that quantifies the propensity of a structural element to buckle, defined by its geometric and material properties, such as width-to-thickness ratio and yield strength. For a plate element:

$$\lambda = \frac{b}{t}\sqrt{\frac{F_y(12)(1-\nu^2)}{\pi^2 Ek}} \tag{1}$$

Where $b$ and $t$ are the plate width and thickness, respectively, $F_y$ is the material yield stress, $E$ is the modulus of elasticity, $\nu$ is the Poisson's ratio and $k$ is a plate buckling coefficient related to the boundary conditions. Slenderness plays a critical role in stability. Higher slenderness leads to early local buckling and reduced energy dissipation (Grondin et al., 1998; Fukumoto and Kusama, 1985). Conversely, lower slenderness ratios enhance energy dissipation and delay buckling, which is essential for seismic resilience. Grondin et al. (1998) found that as plate slenderness increases, the load-carrying capacity decreases, and the likelihood of local buckling rises. This reduction in capacity is also associated with changes in the mode of failure, shifting from stable post-buckling behavior (e.g., Euler buckling) to less desirable forms like plate buckling.

Cyclic loading accelerates stiffness degradation and strain accumulation in structural members due to cyclic plasticity, residual stresses, and the Bauschinger effect. Fukumoto and Kusama (1985) found that thin-walled plates experience significant stiffness loss and energy dissipation after local buckling, driven by residual stresses and local deformation. Yao et al. (2016) similarly observed that cyclic loading reduces in-plane rigidity and increases residual deformation, compromising the plate's overall load-carrying capacity. The Bauschinger effect that reduces yield stress during load reversal amplifies localized buckling as well as the residual bending deformations under reverse cyclic loading, worsening deformation in weakened areas (Goto et al., 1995).

To mitigate these risks, AISC specifications provide slenderness limits for cross-sectional elements. AISC 360 (AISC, 2022b) classifies steel elements (like webs and flanges) based on slenderness to predict their resistance to local buckling. For seismic design per AISC 341 (AISC, 2022a), additional classifications ("highly ductile" and "moderately ductile") aim to ensure large deformations under cyclic loads, but their performance objectives and limits lack consistency and experimental validation. This research aims to enhance the accuracy of predicting the onset of buckling under seismic loading by developing a detailed mechanics-based finite element model. Using ABAQUS, the study investigates the buckling behavior of individual steel plates under inelastic cyclic loading, considering the effects of slenderness, boundary conditions, and cyclic loading protocols. Plates were analyzed using different material models and boundary conditions, and imperfection shapes were defined based on initial buckling modes from linear elastic analyses. These findings provide crucial insights into buckling mechanisms, contributing to the refinement of AISC seismic compactness criteria and ensuring more reliable and consistent seismic

performance of steel structures. This paper outlines the methodology, key findings, and their implications for seismic design.

## 2. Modeling Details

A parametric study was performed on plate elements in order better understand the buckling response of plates under cyclic inelastic loading, and to investigate the effect of various parameters. The finite element modeling was conducted using ABAQUS (ABAQUS, 2023), following methodologies outlined in related studies such as Torabian and Schafer (2014). The model geometry consisted of a rectangular steel plate with dimensions of 250 mm in length and 50 mm in width, representing an aspect ratio of 5:1. To investigate the effects of slenderness, varying thicknesses were applied. The slenderness parameter was calculated with Eq. 1. The plates were meshed using 4-node linear shell elements with reduced integration and hourglass control (S4R in ABAQUS). Models were meshed with maximum finite element dimensions of approximately 2 mm per side. Further mesh refinement did not yield appreciable differences in element behavior.

Four boundary condition configurations were modeled to investigate the effect of boundary conditions of plate ductility. Unstiffened plates, which are supported on one longitudinal side and free on the other, were analyzed with both simple (rotation free) and clamped (rotation fixed) boundary conditions on the supported side. Flanges in wide flange steel members are considered to be unstiffened elements, supported by the web on one side and free on the other. Similarly, stiffened plates, which are supported on both longitudinal sides, were also analyzed with simple and clamped boundary conditions. Webs of wide flange members and walls of square and rectangular HSS members are examples of stiffened elements. These boundary conditions were incorporated into the finite element models by appropriately constraining or releasing degrees of freedom (DOF) along specific edges of the plate, see Figure 1.

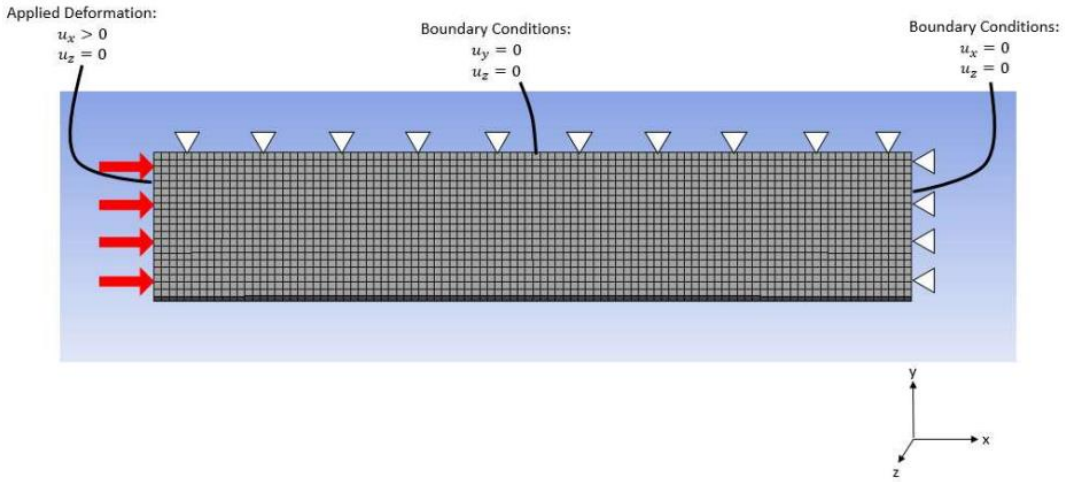


Figure 1: Finite Element Mesh and Boundary Conditions for Unstiffened Plate with Simple Support

Loading was applied to each plate using specified displacement of the nodes on the left side of the plate. In addition to monotonic compression, several cyclic loading protocols were applied: (1) symmetric loading with constant amplitude displacement cycles, denoted as $\pm 4dy$ and $\pm 15dy$, where $dy$ is the yield displacement of the plate, (2) a gradually increasing symmetric loading protocol, denoted as SLP, which is based on the loading protocol utilized for full-scale HSS brace

specimen as described in Kaldestad (2022), and (3) a specialized protocol called $\pm 4dyF$, which involved applying only half the cycles that led to buckling from the standard $\pm 4dy$ loading protocol, and then applying a monotonically increasing compression up to buckling initiation, see Figure 2 where the displacement (U) normalized by the yield displacement ($dy$) is on the Y-axis and the number of half-cycles is on the X-axis. Additionally, to interrogate the effect of initial loading direction, loading protocols with one tension excursion followed by compression to the point of buckling were applied.

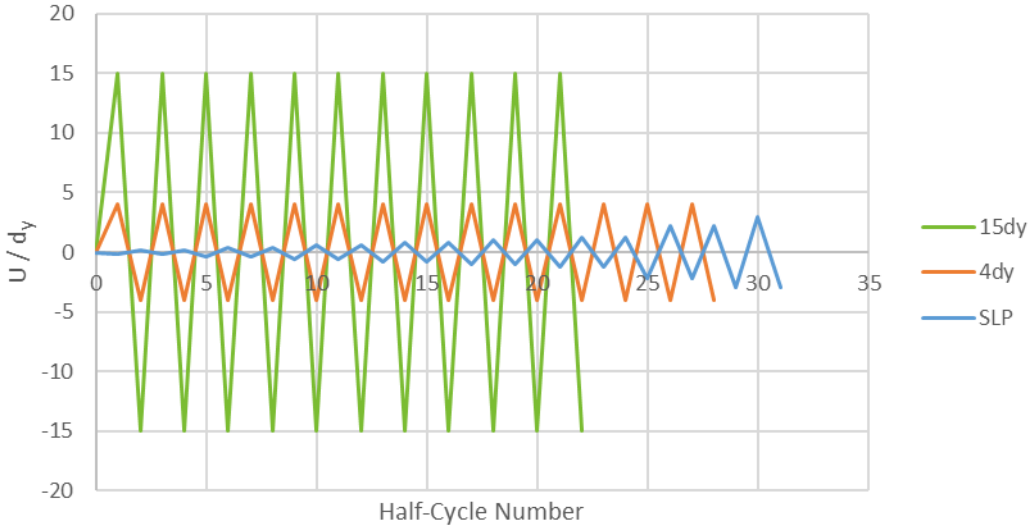


Figure 2: Loading Protocols

The cyclic hardening behavior of the material was modeled using ABAQUS's built-in cyclic plasticity framework. This approach employs a von Mises yield criterion combined with isotropic and kinematic hardening, based on the Armstrong and Frederick (1966) model. A single backstress term represents kinematic hardening, while isotropic hardening was captured through an exponential model. The hardening parameters used in the study were based on calibrated parameters for A500 Grade C steel, from Kaldestad (2022). Three material model calibrations were utilized to explore the influence of minor variations in hardening properties on buckling performance under cyclic loading. The material model calibration parameters are given in Table 1.

Table 1: Material Model Calibrations

| Material Calibration[1] | Yield Stress (MPa) | $Q_\infty$ (MPa) | b | $C_1$ (MPa) | $\gamma_1$ |
|---|---|---|---|---|---|
| 1 | 469 | 69 | 6 | 2068 | 25 |
| 2 | 448 | 51.7 | 5 | 3000 | 30 |
| 3 | 448 | 207 | 3 | 2896 | 35 |

1. All calibrations utilized E=200,000 MPa and ν=0.3.

Imperfections were introduced into the model to replicate realistic initial deviations from flatness, which may trigger buckling under sufficient deformation. The imperfection shapes were defined based on the first buckled mode shape obtained from a linear elastic buckling analysis. The maximum imperfection amplitude was calculated using the equation:

$$\omega_0=\gamma\lambda^2/t \quad (2)$$

where $\omega_0$ is the imperfection amplitude, $\gamma$=0.066 based on the recommendations in Torabian and Schafer (2014), $\lambda$ is the slenderness parameter, and $t$ is the plate thickness. The results from the parametric studies, which included varying slenderness ratios, material properties, boundary conditions, and loading protocols, were utilized to develop a simplified analytical model, which may predict the buckling behavior of steel plates under cyclic loading, contributing to the broader goal of enhancing seismic design criteria.

Table 2 Parametric Variation

| Parameter | Value | Notes |
|---|---|---|
| Slenderness ($\lambda$) | 0.2-0.6 | |
| Plate buckling coefficient ($k$) | 0.425 | Unstiffened plate, simple BC |
| | 1.227 | Unstiffened plate, clamped BC |
| | 4.0 | Stiffened plate, simple BC |
| | 6.97 | Stiffened plate, clamped BC |
| Material model calibrations | 3 | See Table 1 |
| Loading protocols | 1 monotonic | See Figure 2 |
| | 4 cyclic | |

The analysis procedure for each plate involved multiple steps. First, a linear elastic buckling analysis was performed to identify the buckling modes and determine the initial imperfection shapes. Subsequently, nonlinear static analyses were conducted to capture the inelastic buckling response under cyclic loading. The primary outputs recorded during each analysis include: (1) applied displacement, (2) the total reaction force, (3) the applied displacement and cycle number at the initiation of buckling. The buckling point in each analysis was identified from the global force-displacement response as the point in the when the applied force reached a maximum under increasing compressive displacement. Figure 3a shows the buckling point under monotonic loading and Figure 3b shows the buckling point under cyclic loading for a representative specimen. Under monotonic loading, the applied displacement at buckling initiation may be normalized by the displacement at yielding:

$$\beta_{mono} = \frac{\delta_m}{\delta_y} \quad (3)$$

From previous works of Torabian and Schafer (2014), this value can be related to the non-dimensional slenderness parameter, $\lambda$. For cyclic loading, several additional metrics were calculated to evaluate the cyclic buckling response, including cumulative compressive displacement and cumulative compressive plastic displacement. Cumulative compressive displacement is defined as:

$$\delta_{cc} = \sum_{i=1}^{n} \delta_{i,c} \quad (4)$$

Where $\delta_{i,c}$ is the compressive deformation applied during cycle *i*, and *n* is the total number of load cycles up to and including the initiation of buckling. Reporting the capacity in this manner is instructive, as the cumulative deformation provides information on the total seismic energy dissipated by the component prior to buckling. This value may also be normalized by the yield displacement to determine $\beta_{cyclic}$, the normalized cumulative compressive displacement.

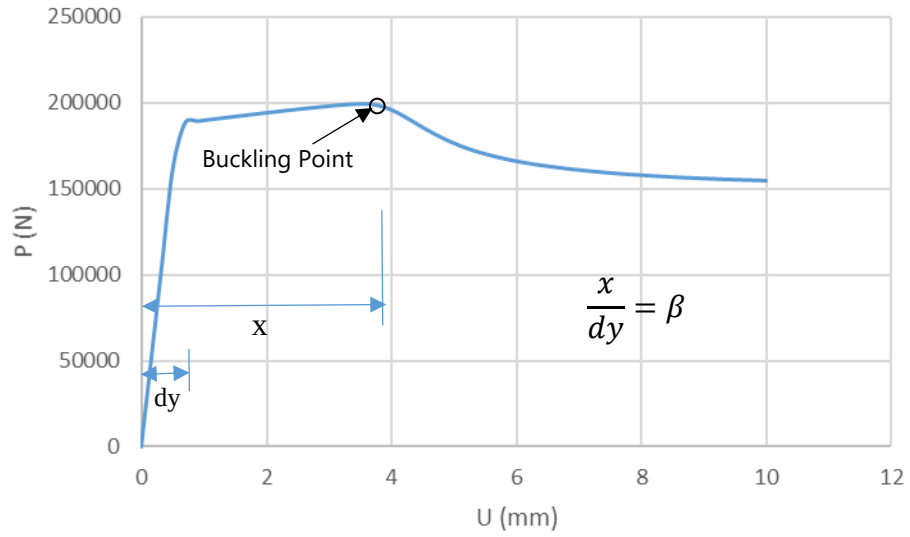


(a)

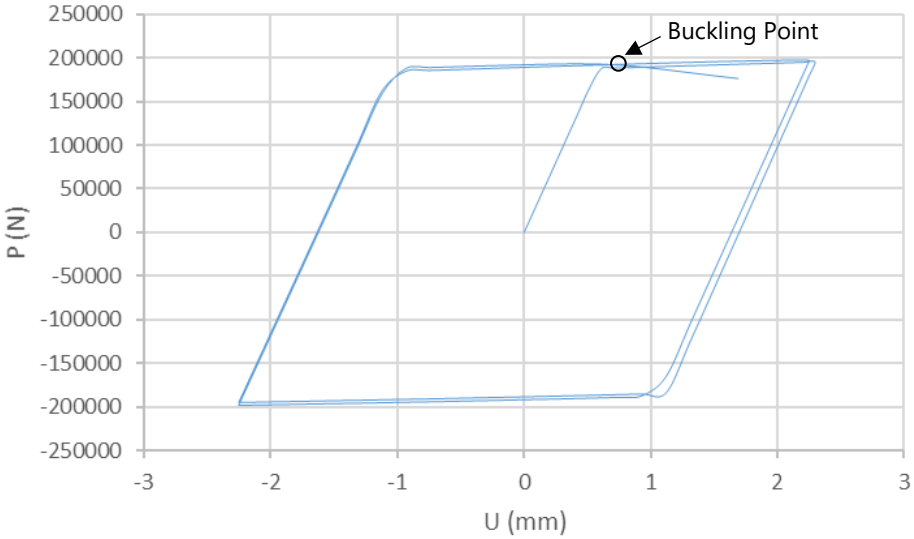


(b)

Figure 3: Force-Displacement Response of (a) Monotonic Specimen and (b) Cyclic Specimen

## 3. Results of parametric study

After completing the parametric study, the results were analyzed to determine trends and to guide the development of the predictive model for inelastic cyclic buckling. General results will be presented in this section, followed by a detailed discussion on the developed model.

### *3.1 Monotonic Results*

The monotonic loading protocol served as a baseline for assessing the buckling behavior of steel plates by applying a gradually increasing compressive load until failure. The results of the monotonic specimens are shown in Figure 4, where slenderness is plotted on the horizontal axis and $\beta_{mono}$ is plotted on the vertical axis. Each marker in the figure represents a single analysis,

and markers are color-coded by boundary conditions. Plates with lower slenderness ratios were observed to exhibit higher cumulative displacement capacities before buckling, while slender plates experienced early instability. These findings align with those of Torabian and Schafer (2014), who similarly observed a similar trend. Their expression for $\beta_{mono}$ for elastic-perfectly plastic material is also included in Figure 4 for reference.

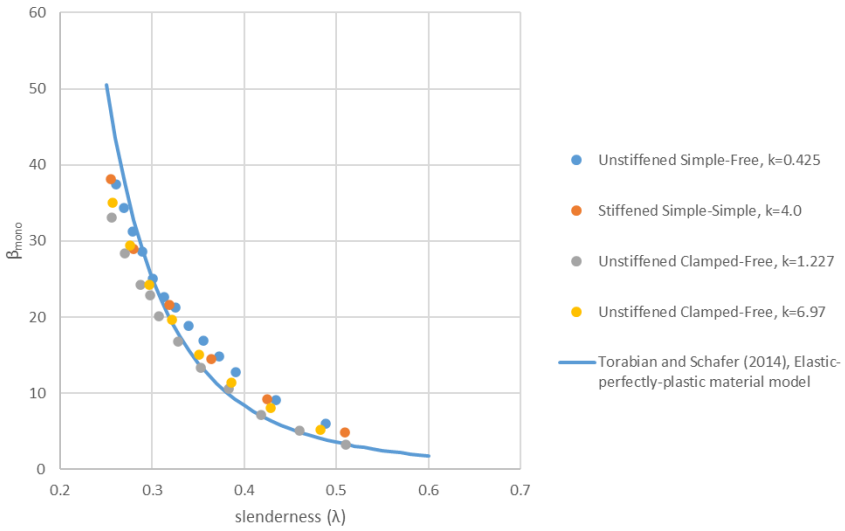


Figure 4: Monotonic Specimen Response

*3.2 Cyclic Results*

*3.2.1 Results by loading protocol*

Results from the unstiffened cyclic specimens with simple boundary conditions are shown in Figure 5, where slenderness is plotted on the horizontal axis and $\beta_{cyclic}$ is plotted on the vertical axis. Markers are color coded by the cyclic loading protocol. As can be observed from the figure, the same qualitative trend applies regardless of loading protocol (increasing deformation capacity with decreasing slenderness). However, $\beta_{cyclic}$ displays an apparent dependence on loading protocol.

For example, the results from the SLP approach the 4dy loading protocol results for most of the range of slenderness values considered. However, as the slenderness decreases, the SLP results begin to shift toward those observed in the 15dy loading protocol. This behavior can be attributed to the gradual increase in cycle amplitude inherent in the SLP. At later cycles, the strain amplitudes become significantly larger, diminishing the influence of earlier, smaller cycles. Consequently, the SLP results become more comparable to the 15dy protocol, where large-amplitude cycles dominate the overall displacement response, see Figure 5. Also, it is observed that larger cycles, such as cycles from the 15dy loading protocol, result in reduced cumulative displacement capacity.

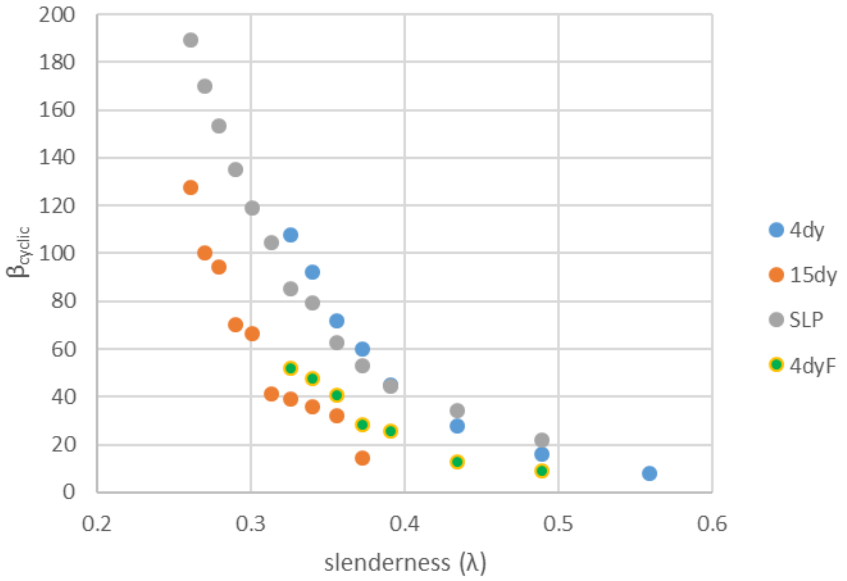


Figure 5: Unstiffened Simple-Free Plate Under Different Loading Protocols

*3.2.2 Boundary Conditions*

Cyclic loading showed that the strain capacity and buckling initiation were not significantly influenced by the boundary conditions similar to the previous results from monotonic. Although boundary conditions, such as clamped or simply supported edges, play a role in controlling lateral displacements and stress redistribution, their effect on the cumulative displacement $\beta_{cyclic}$ and the buckling initiation remained limited across different protocols.

As shown in Figure 6, $\beta_{cyclic}$ for plates with varying boundary conditions align closely. For instance, the differences between the clamped-clamped (stiffened) and simple-free (unstiffened) configurations remained within an acceptable range, even under large-amplitude cycles like ±15dy. This suggests that the impact of boundary conditions appears to be well-captured by the parameter slenderness, λ.

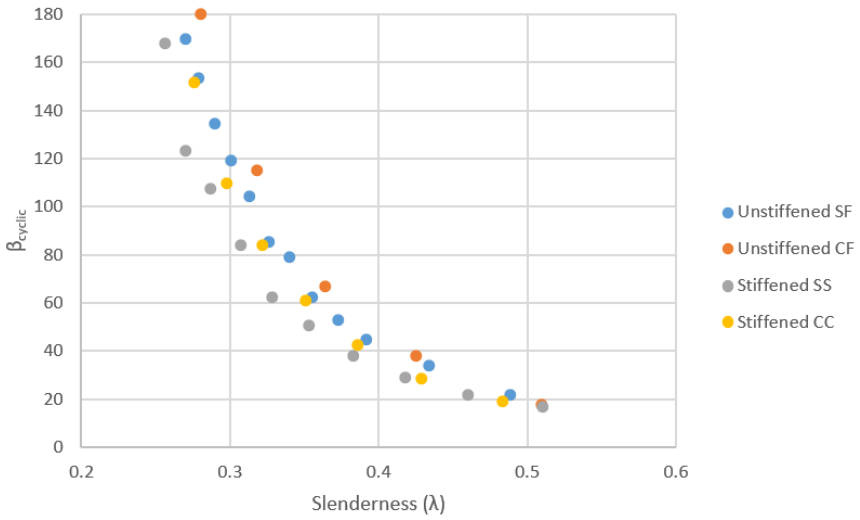


Figure 6: Influence of Different Boundary Conditions on Cyclic Loading

*3.2.3 Material Parameter Variation*

The material models in commercial FE programs are often very accurate, but they can take many parameters as input. When calibrating material model parameters to coupon experiments, oftentimes only global data (force-displacement) is available for the coupons, not stress and strain. Since the global experimental data includes the combined effects of geometric nonlinearity (buckling, necking, etc.) and material nonlinearity, obtaining a unique set of constitutive parameters which can accurately simulate the material response can challenging. Often, many different parameter sets result in similar overall response. To investigate this effect, different material model calibrations which attempt to represent the same material (in terms of $F_y$ and $F_u$) were utilized, in order to interrogate this effect.

Interestingly, slight changes in material parameters (e.g., yield stress, strain hardening properties) had only a minimal impact on the results. For instance, plates analyzed with modified materials (referred to as Mat2 and Mat3) exhibited $\beta_{cyclic}$ values that deviated only marginally from the baseline material, see Figure 7, where the differences between materials are observed to be 5% or less. This consistency suggests that plate geometry and loading conditions have a more pronounced influence on buckling behavior than minor material variations.

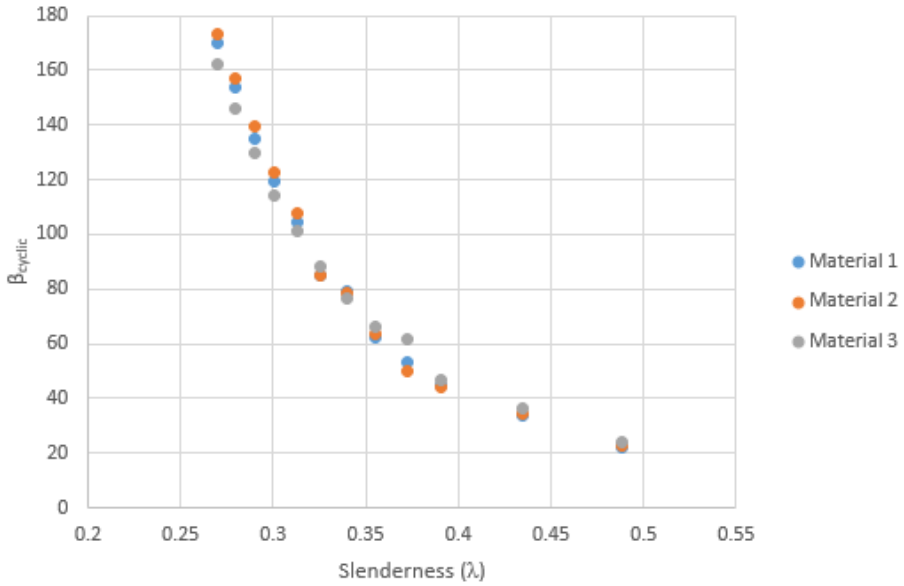


Figure 7: The Influence of Different Materials Models on $\beta_{cyclic}$ for Diferent Slenderness

*3.2.4 Effect of tension before compression*

In this study, we also examined the impact of applying tension cycles of varying magnitudes (+2dy, +4dy, +6dy, +8dy, +10dy, +12dy and +15dy) before compressing plates to failure. The results show that the magnitude of the initial tension cycle significantly influences the plate's behavior during subsequent compression. For all configurations tested, larger tension cycles generally increased the plate's ability to sustain subsequent compressive displacement before buckling. For example, unstiffened plates with simple-free boundary conditions demonstrated that as the magnitude of the tension cycle increased (e.g., from (+2dy) to (+15dy)), $\beta$ consistently increased. Similarly, stiffened plates with simple-simple or clamped-clamped

boundary conditions showed greater buckling resistance under larger tension cycles. This effect was incorporated into the developed analytical model (see Section 4.1).

## 4. Analytical model to predict buckling under cyclic loading

### *4.1 Model development*

Based on a review of the results, a preliminary functional form for an analytical model to predict the onset of buckling was developed, along with a preliminary attempt to calibrate the model parameters. Given the results presented in the section above, it is important that the model incorporate the effects of loading history. Borrowing from concepts in continuum fracture mechanics, one possible form of the model is shown below:

$$B = \int_{\varepsilon_{comp}} f(x_1, x_2, x_3 \ldots)\, d\varepsilon - \int_{\varepsilon_{tens}} g(x_1, x_2, x_3 \ldots)\, d\varepsilon \tag{5}$$

Where $B$ is a scalar index ranging from 0 to 1, with a value of $B$=0 at the beginning of loading and a value of $B$=1 when buckling is predicted. The first term represents an integration over each compressive strain increment and the second term represents and integration over each tensile strain increment. Under compressive loading increments, the index increases towards the critical value of 1, and during tensile loading cycles, the index reduces. Thus, load history is included directly in the model formulation. This functional form also reflects observations of the plate simulations with tension applied first which suggest that large tension excursions can be beneficial in terms of increasing the cumulative amount of compressive strain that the plate can withstand.

Preliminary expressions for $f(x_1, x_2, x_3 \ldots)$ and $g(x_1, x_2, x_3 \ldots)$ were developed. These can be seen in Eq. 5. The parameters which impact the buckling prediction include $\beta_{mono}$, the monotonic deformation capacity, and a constant c*, which quantifies the rate of decrease of the buckling index during tension cycles.

$$B = \int_{\varepsilon_{comp}} \frac{1}{\beta_{mono}\varepsilon_y}\, d\varepsilon - \int_{\varepsilon_{tens}} \frac{c^*}{\beta_{mono}\varepsilon_y}\, d\varepsilon \tag{6}$$

After introducing the general form, modifications to the model were developed. During calculation of the buckling index, the elastic unloading portions of both tension and compression cycles within any loading protocol were excluded. As a result, $\beta_{mono}$ was adjusted to reflect the plastic monotonic strain capacity only. These adjustments were found to significantly improve the predictive capability of the model. The improvement was attributed to better accounting for the Bauschinger effect. By incorporating these adjustments, our method provides a robust mechanism for predicting the onset of buckling under complex cyclic loading conditions.

To enhance the prediction even more we introduced two parameters, $C_1$ and $C_2$. The first parameter, $C_1$, was introduced to modify the contribution of displacement values in the buckling index that are coming from the tension cycles. Tension displacements typically arise from the reverse cycles in the loading protocol, and their unadjusted magnitude overestimate the damage accumulation. By multiplying tension displacements by $C_1$, their impact was proportionally reduced to better reflect their contribution to the overall buckling process. However, this adjustment alone was not sufficient in cases where $B$ dropped below zero during the damage progression.

To address this, the second parameter, $C_2$, was introduced as an additional correction factor to better predict the initiation of buckling. When $B$ turned negative, $C_2$ was applied to further adjust the negative displacements, ensuring that the sum reflected a more realistic progression toward buckling. Thus, in the context of Eq. 3, the parameter c* may be defined as:

$$c^* = \begin{cases} C_1 \; when \; B \geq 0 \\ C_2 \; when \; B < 0 \end{cases} \tag{7}$$

By iteratively refining the values of $C_1$ and $C_2$, we aimed to bring the value of $B$ at buckling as close as possible to a target value of 1 across all loading protocols for a given specimen. This method provided a generalized and adaptable framework for assessing buckling behavior across different cyclic loading scenarios, making it a valuable tool for predicting structural performance in practical applications.

As an example, Figure 8 displays the evolution of the buckling index over the applied loading history of each unstiffened, simple-free simulation with $\lambda_l$=0.349. The yellow line labeled as "Near Fault" corresponds to the tension-first loading protocol used in this study, see Section 2. The onset of buckling in each simulation is indicated with a marker, and the value of the index at buckling can be read from the vertical axis. As can be seen, all values fall in the range of $0.9 < B < 1.1$ at the occurrence of buckling, regardless of loading protocol. This suggests that the preliminary model can predict the occurrence of buckling in a variety of plate geometries with reasonable accuracy while incorporating the effects of loading history.

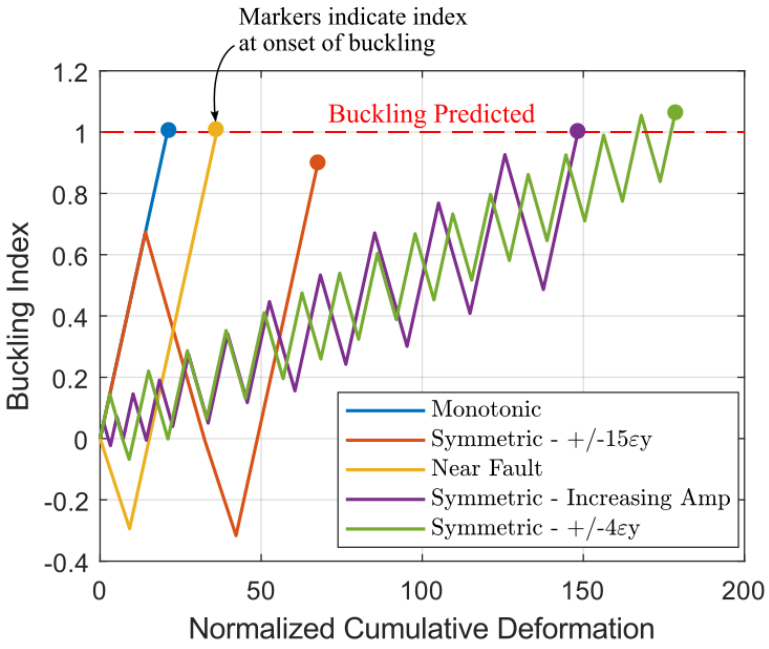


Figure 8: Buckling Index Evolution for Analyses with $\lambda_l$=0.349

*4.2 Model calibration*

To verify the generality of the proposed methodology, we incorporated the additional loading protocols from the tension effect discussed in Section 2. These loading protocols introduced pre-

tension cycles of varying magnitudes before compression to failure. This allowed us to evaluate whether the predictive framework could reliably estimate the initiation of buckling across different highly non-proportional and asymmetric loading scenarios.

Additionally, to refine the prediction process, we developed a MATLAB code to calculate the optimal values of $C_1$ and $C_2$ using five representative loading protocols. The code iteratively adjusted these parameters to minimize the average error in the prediction of the buckling index:

$$\epsilon_j = \frac{1}{n}\sum_{i=1}^{n}\left|B_{i,j} - 1\right| \tag{8}$$

Where $B_{i,j}$ is the calculated buckling index at the point of observed buckling in specimen *i* with trial parameter set *j*, and $\epsilon_j$ is the error over all *n* specimens for trial parameter set *j*. To test the generality of these optimized values, the $C_1$ and $C_2$ parameters were then applied to a separate set of three different loading protocols. The results showed that the predicted values of *B* for these additional protocols within a range of +/-15% error, demonstrating the robustness of the methodology. The loading protocols in Table 1, labeled as Calibration Loading Protocols, represent the cases used to derive the optimal $C_1$ and $C_2$ values. These values were subsequently tested on the loading protocols labeled as Predictions, further verifying the model's accuracy and adaptability.

Table 3: Calibration Results for Select Unstiffened (Simple Free) Cases

| λ | Calibrated Parameters | | Value of *B* at buckling Calibration loading protocols | | | | | Value of *B* at buckling Predictions | | |
|---|---|---|---|---|---|---|---|---|---|---|
| | $C_1$ | $C_2$ | 4dy | SLP | 15dy | TE+10dy | TE+15dy | 4dyF | TE+2dy | TE+4dy |
| 0.434 | 0.61 | 0.4 | 1.07 | 0.87 | - | 1.04 | 1.05 | 1.07 | 1.01 | 0.88 |
| 0.373 | 0.69 | 0.5 | 1.07 | 0.93 | - | 0.96 | 1.02 | 0.89 | 0.98 | 0.96 |
| 0.356 | 0.7 | 0.4 | 1.13 | 0.88 | - | 1.05 | 1.03 | 0.97 | 0.93 | 0.98 |
| 0.34 | 0.73 | 0.4 | 1.13 | 0.85 | 1.03 | 1.04 | 1.04 | 0.99 | 0.98 | 0.98 |

However, manual evaluation of $C_1$ and $C_2$ revealed certain limitations of the automated optimization process. While the MATLAB code effectively minimized the total error across all protocols, it sometimes allowed large individual errors for specific cases while keeping the total error low. For instance, the error for some loading protocols exceeded 20%, even when the overall error was acceptable. By manually adjusting $C_1$ and $C_2$, we distributed the errors more evenly across the different protocols, achieving a more balanced and accurate prediction framework, see Figure 9. The approach not only accounts for various boundary conditions and preloading effects but also adapts to the nuances of different loading protocols, making it a valuable tool for structural performance analysis.

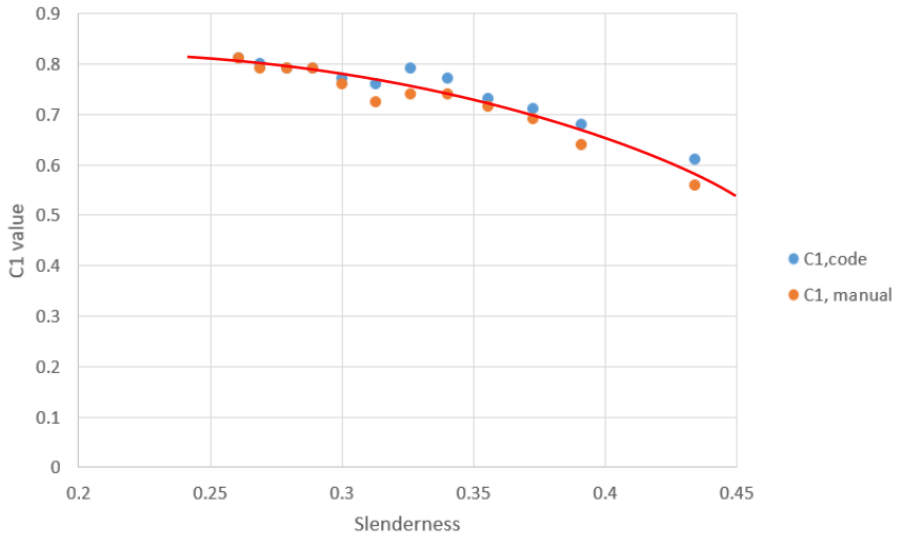


Figure 9: Comparison Between Evaluating C1 Using the MATLAB Code and Manual Trial

*4.3 Sensitivity of calibration*

To analyze the sensitivity of the buckling prediction methodology to variations in $C_1$ and $C_2$ , we created contour plots with $C_1$ values represented on the horizontal axis, $C_2$ values on the vertical axis, and the average error from all loading protocols depicted on the contour levels. The average error measures how far the predicted *B* is from the target value of 1, averaged across multiple loading protocols.

The contour plots allowed us to visualize how different combinations of $C_1$ and $C_2$ affect the accuracy of the predictions. In regions where the average error was close to zero, the predictions across all protocols were well-aligned with the target value of 1. Areas with larger average errors highlighted parameter combinations that produced less accurate predictions, often due to overestimations or underestimations of contributions from specific loading protocols.

The contour plots also revealed that, in most cases, the error in the prediction was more sensitive to changes in $C_1$ compared to $C_2$. Variations in $C_1$ significantly influenced the average error, indicating that adjustments to the tension-related parameter had a more pronounced impact on the prediction accuracy, as shown in Figure 10. In contrast, changes in $C_2$ generally resulted in errors within the same range, suggesting that the cumulative correction applied by $C_2$ is less critical to the overall accuracy in many scenarios. This indicates that the prediction methodology relies more heavily on $C_1$ to capture the displacement contributions effectively, while $C_2$ adjustments provide stability but with a relatively lower sensitivity.

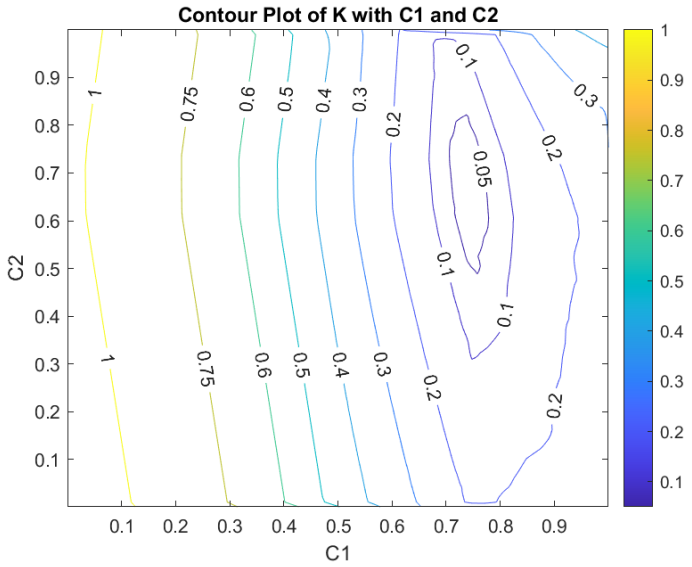

Figure 10: Contour Plot from Unstiffened Simple Free Boundary Condition with $\lambda$ = 0.31

## 5. Conclusions

This study investigated the initiation of local buckling in steel plates under cyclic loading and developed a predictive methodology using mechanics-based modeling. The findings and conclusions derived from this work are summarized as follows:

- Loading protocol was found to have a major impact on cumulative displacement at buckling. Specimens loaded with small strain amplitude cycles were able to sustain greater cumulative displacements prior to buckling as compared to specimens loaded under larger strain amplitude cycles
- Symmetric Loading Protocols (SLP) provided predictions consistent with monotonic buckling results at higher slenderness ratios.
- At lower slenderness ratios, SLP results closely resembled the 15dy loading protocol, where larger cycle amplitudes dominated the cumulative displacement.
- Pre-tension cycles (+2dy to +15dy) delayed buckling initiation and increased displacement capacity, demonstrating a beneficial effect of tension delaying buckling.

Role of Slenderness and Boundary Conditions:

- Higher slenderness ratios led to earlier buckling initiation, under both monotonic and cyclic loading.
- The non-dimensional slenderness parameter, λ, was found to provide a robust characterization of effective slenderness, taking into account boundary conditions.

Material Properties:

- Variations in constitutive calibration had minimal impact on buckling initiation, emphasizing the dominance of geometric factors.

Predictive Model Parameters C1 and C2:

- C1 adjusted the contribution of tension displacements to account for overestimated buckling index accumulation.
- C2 corrected the buckling index when it turned negative, ensuring alignment with realistic damage progression.
- Optimal C1 and C2 values predicted buckling within a 15% error range for new loading protocols.
- Manual adjustments distributed errors more evenly across protocols, addressing limitations of automated optimization.

Sensitivity Analysis:

- Prediction error was more sensitive to variations in C1 than C2, highlighting the importance of tension-related adjustments.
- Contour plots identified C1 and C2, combinations, minimizing average error across protocols.

This study presents a comprehensive and generalized framework for predicting the initiation of buckling in slender steel plates under cyclic loading, regardless of the specific loading protocol or loading history. The methodology integrates key factors, including cyclic plasticity and boundary conditions effects, to ensure reliable predictions. Future work will expand on these findings by integrating experimental studies to validate the computational models. Another avenue for future research involves exploring the influence of advanced material models, such as high structural strength steels and non-conventional materials like stainless steel. Building on the preliminary findings, this project aims to develop a mechanics-based Appendix to AISC 341, providing an alternative methodology for assessing local buckling resistance under seismic loading conditions.

**Acknowledgments**

This work was supported by the American Institute of Steel Construction (AISC) and the North Carolina State University College of Engineering.

**References**

AISC (2022a). Seismic Provisions for Structural Steel Buildings, ANSI/AISC 341-16, American Institute of Steel Construction, Chicago, IL.

AISC (2022b). Specification for Structural Steel Buildings, ANSI/AISC 360-16, American Institute of Steel Construction, Chicago, IL.

Armstrong, P. J., & Frederick, C. O. (1966). A mathematical representation of the multiaxial Bauschinger effect (Vol. 731). Berkeley, CA: Berkeley Nuclear Laboratories.

ABAQUS (2023) ABAQUS User's Manual. Simulia. Providence, RI.

Bradfield, C. D. (1980). "Tests on plates loaded in in-plane compression." *Journal of Constructional Steel Research*, Prof Publishing, 1(1), 27–37. https://doi.org/10.1016/0143-974X(80)90006-1

Fell, B. V., Kanvinde, A. M., Deierlein, G. G., & Myers, A. T. (2009). "Experimental investigation of inelastic cyclic buckling and fracture of steel braces." *Journal of Structural Engineering*, Prof Publishing, 135(1), 19–32. https://doi.org/10.1061/(ASCE)0733-9445(2009)135:1(19)

Fukumoto, Y., & Kusama, H. (1985). "Cyclic behaviour of plates under in-plane loading." *Engineering Structures*, Prof Publishing, 7(1), 56–63. https://doi.org/10.1016/0141-0296(85)90037-9

Goto, Y., Toba, Y., & Matsuoka, H. (1995). "Localization of plastic buckling patterns under cyclic loading." *Journal of Engineering Mechanics*, Prof Publishing, 121(4), 493–501. https://doi.org/10.1061/(ASCE)0733-9399(1995)121:4(493)

Grondin, G. Y., Chen, Q., Elwi, A. E., & Cheng, J. J. (1998). "Stiffened steel plates under compression and bending." *Journal of Constructional Steel Research*, Prof Publishing, 45(2), 125–148. https://doi.org/10.1016/S0143-974X(97)00058-8

Kaldestad, J. (2022). "Experimental Investigation into the Cyclic Response of A1085 HSS Braces." Master's Thesis, University of Washington, Seattle, WA.

Torabian, S., & Schafer, B. W. (2014). "Role of local slenderness in the rotation capacity of structural steel members." *Journal of Constructional Steel Research*, Prof Publishing, 95, 32–43. https://doi.org/10.1016/J.JCSR.2013.11.016

Yao, T., & Fujikubo, M. (2016). "Buckling/plastic collapse behavior and strength of rectangular plate subjected to uni-axial thrust." *Buckling and Ultimate Strength of Ship and Ship-Like Floating Structures*, Prof Publishing, 75–155. https://doi.org/10.1016/B978-0-12-803849-9.00004-6